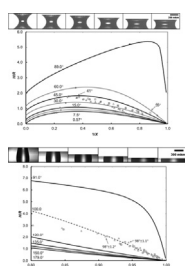# Statics and dynamics of capillary bridges

Plamen V. Petkov [a],[*], Boryan P. Radoev [b]

[a] Sofia University "St. Kliment Ohridski", Faculty of Chemistry and Pharmacy, Department of Physical Chemistry, 1 James Bourchier Boulevard, 1164 Sofia, Bulgaria
[b] Sofia University "St. Kliment Ohridski", Faculty of Chemistry and Pharmacy, Department of Chemical Engineering, 1 James Bourchier Boulevard, 1164 Sofia, Bulgaria

HIGHLIGHTS

- The study pertains both static and dynamic CB.
- The analysis of static CB emphasis on the 'definition domain'.
- Capillary attraction velocity of CB flattening (thinning) is measured.
- The thinning is governed by capillary and viscous forces.

GRAPHICAL ABSTRACT

ARTICLE INFO

ABSTRACT

The present theoretical and experimental investigations concern static and dynamic properties of capillary bridges (CB) without gravity deformations. Central to their theoretical treatment is the capillary bridge definition domain, i.e. the determination of the permitted limits of the bridge parameters. Concave and convex bridges exhibit significant differences in these limits. The numerical calculations, presented as isogones (lines connecting points, characterizing constant contact angle) reveal some unexpected features in the behavior of the bridges. The experimental observations on static bridges confirm certain numerical results, while raising new problems of interest related to the stability of the equilibrium forms.

The dynamic aspects of the investigation comprise the capillary attraction (thinning) of concave bridge. The thinning velocities at the onset of the process were determined. The capillary attraction, weight of the plates and viscous forces were shown to be the governing factors, while the inertia forces turned to be negligible.

1. Introduction

The modern basis of capillary bridges investigation was set with the studies of Plateau, who 140 years ago defined a mathematical problem, known nowadays as Plateau's problem [1]. Defined originally as a purely mathematical issue (finding the surface with minimal area at given boundaries), it has turned in the years into an analytical tool for the description of capillary systems. Ever since the second half of the last century, capillary bridges (CB) have been among the intensively studied capillary systems. It corresponds to their increasing application in laboratory techniques and industrial praxis. For example: liquid material transferring from AFM tips to silicone substrates for lithographic purposes [2]. With the development of patterning and lithography studies of capillary bridges in slit pore geometry became important [3]. Further implementation of CB can be found in the so-called weakly adhesive solid surfaces studies [4]. CB between two bodies of spherical shape appears to be important for soil–water interaction. Interesting are the investigations of surface roughness influence on the CB behavior [5].

* Corresponding author. Tel.: +359 28161668.
E-mail addresses: pvpetkov@lcpe.uni-sofia.bg, pvpetkov@yahoo.com (P.V. Petkov).

P.V. Petkov, B.P. Radoev / Colloids and Surfaces A: Physicochem. Eng. Aspects 460 (2014) 18–27

19

There have been attempts to develop methods for contact angles measurement between the liquid and two particles [6].

The recent CB theoretical investigations primarily feed the experiment (see above), but attention is also paid to classical problems like equilibrium, stability, etc. [7–9].

Our study pertains to both the experiment and the theory of CB. In theoretical aspects the relations between CB geometrical parameters are investigated mainly (contact radius, height, contact angle, etc., Section 3). The emphasis is on the so-called 'definition domain', e.g. the upper CB height limit at given contact angle and volume. Some dynamic characteristics are also considered, such as the capillary pressure and CB-maintaining external force. The experimental part (Section 2) describes the setup and methods for measuring equilibrium (static) and nonequilibrium (dynamic) CB states. The new moment here is the measured velocity of mutual approach of the CB plates upon acting of capillary attraction. The analysis of the dependence 'attraction (thinning) velocity vs. CB height' clearly shows that the inertia forces are negligible, as compared to the drag forces. In Section 4, the main experimental results are presented, as well as their interpretation. The work is completed with concluding remarks (Section 5). Some mathematical details are incorporated as an appendix.

2. Experimental setup

Our experimental setup consists of a micrometer, onto the measuring arms of which two square ($20\,mm \times 20\,mm \times 2\,mm$) stainless steel supporting plates were fixed parallel to each other.

Two $22\,mm \times 22\,mm$ microscope cover glasses (ISOLAB) of soda lime silica composition were selected as working surfaces. They were glued to the supporting plates for static measurements. In the case of attraction kinetics experiments, only the upper glass was glued, while the lower one was placed on the corresponding stainless steel plate. Images were recorded by using a high-speed camera, MotionXtra N3, which was mounted onto a horizontal optical tube with appropriate magnification (Fig. 1). All experiments were carried out with deionized (Milipore) water.

2.1. Static capillary bridge experiments

Two types of static experiments were performed:

(1) Hydrophilic glass surfaces were pre-cleaned with 99.9% C_2H_5OH and washed with deionized (Millipore) water before being glued to the supporting plates. A small droplet of $\approx 1\,mm^3$ volume, was placed in the middle of the lower glass slide. The upper glass slide was moved toward the droplet until a capillary bridge was formed. Further, several equilibrium states were recorded; pressing the shape until thin film was formed. Afterwards stretching took place until breakage occurred (Fig. 5 presents several consecutive pictures of stretching). The

experiment was repeated several times with varying initial droplet volume. Concerning the effects due to evaporation, the direct volume decrease played no role, since the theoretical relations are CB volume invariant (Section 3.3). Other effects related to the evaporation (e.g. thermo-effects) were not observed.

(2) Experiments with hydrophobized glass cover slides were performed. The preliminary hydrophobization was done with PDMS (Rhodia Silicones, 47V1000), following the procedure developed by Marinova et al. [10]. Before gluing the slides, they were washed with 99.9% C_2H_5OH. The capillary bridge was formed after placing a droplet on the lower surface and attaching it later to the upper glass slide. Stretching was applied onto the droplet until a breakage of the capillary bridge occurred. Selected sequential pictures of the experimental part are presented in Fig. 6.

2.2. Dynamic capillary bridge experiments

A single drop of volume $V \approx 1\,mm^3$ was placed on a hydrophilic glass slide of weight, $m \approx 0.3 \times 10^{-3}\,kg$. Another flat, hydrophilic planar cover glass was moved toward the droplet from above until a CB was formed in an equilibrium state. When the distance between the plates was slightly reduced, by Δh, the lower plate was taken off from the support by the capillary force F_γ and the CB began fast thinning. The recorded data of the dependence h vs. t, are presented in Fig. 7.

3. Mechanical balance and calculations

Our theoretical investigations concern only the mechanical properties of CB. We do not consider the processes of evaporation, condensation and the related potential temperature effects [11–13]. The gravitational deformation of the liquid/gas surfaces is neglected in the theoretical analysis, due to the small linear dimensions of the drop. Yet, in sufficiently stretched CB, especially if hydrophobic, signs of gravitational deformation were observed experimentally, which fact is discussed in Section 4. Here, in Section 3, we shall present separately the mechanical balance of static and dynamic CB.

3.1. Static balance

In general, the CB mechanical equilibrium comprises the pressure balance on liquid/gas interfaces and the external force on the CB plates balancing the capillary attraction/repulsion. Upon neglecting gravity effects and other external fields, the pressure balance is reduced to $\Delta P = P_y = \text{const}$, where $\Delta P = P_i - P_e$ is the jump across the liquid/gas interfaces, P_i, P_e are the internal, external pressures. For CB with axial symmetry; the capillary pressure takes the form $P_y = \gamma r^{-1} \partial(r \sin\varphi)/\partial r$, with γ as the interfacial tension
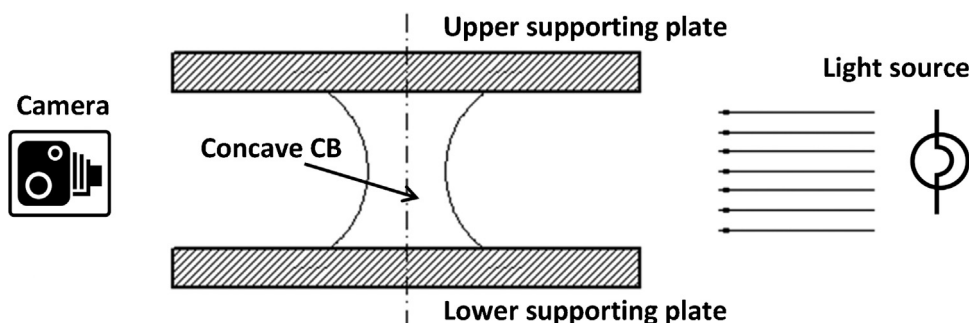

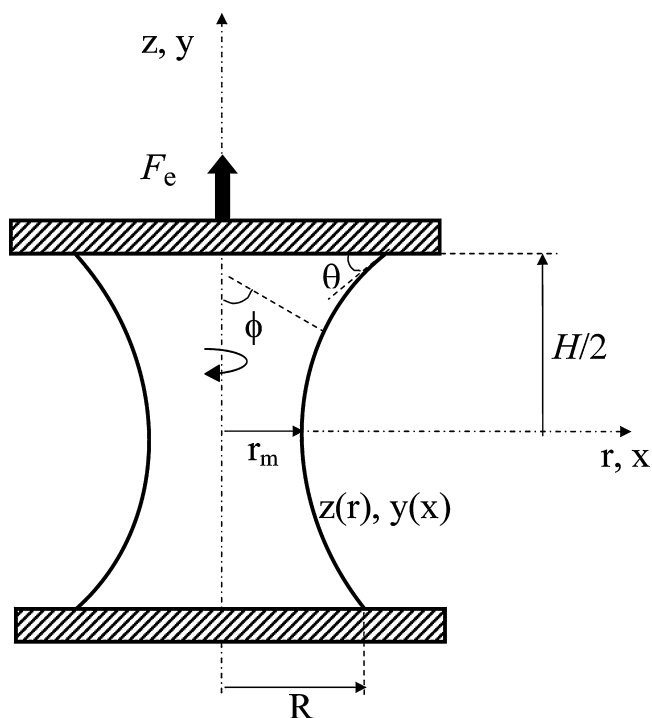**Fig. 1.** Schematic representation of the experimental setup.

Fig. 2. Schematic representation of a concave CB (see Glossary for the denotations).

Fig. 3. Parametrical plot of H/R vs. $1/X$ curves: (A) classical catenoid and (B) CB with zero capillary pressure (catenoidal state). Note the different co-ordinates of the maxima.

liquid/gas, r, as the radial co-ordinate and φ as the angle between the axis of symmetry and the generatrix normal (Fig. 2) [14].

Axial symmetry is justified in this case, as we consider CB formed between parallel and homogeneous plates. The first integral of the pressure balance (in scaled form) offers no difficulty:

$$\sin \varphi = C(x^2 - 1) + 1 \qquad (1)$$

where $x = r/r_m$ is the dimensionless radial coordinate and $0 \leq 1$, $0 \leq \theta < \pi/2$ is the dimensionless capillary pressure. Further on we shall use another scaling parameter, $V^{1/3}$ (V = CB volume), allowing for the liquid incompressibility (for the denotations see Glossary). The neck radius r_m, also used by other authors as scaling parameter [9, Chapter 11], has the advantage of reducing the CB genera-trix equation to a mono parametric curve $y(x, C)$, Eq. (5). Another illustration of the neck radius, useful as a scaling measure, is the expression of C. Applying Eq. (1) to the liquid/solid contact ($x = X$) one obtains:

$$C = \frac{X \sin \theta - 1}{X^2 - 1} \qquad (2)$$

The parameters, $X = R/r_m$, and θ are the dimensionless contact radius and contact angle (Fig. 2).

Relation (2) clearly shows the algebraic character of $C \sim P_\gamma$, i.e. it can be positive, zero or negative. At convex generatrix ($X < 1$), in the entire interval of angles ($\pi/2 < \theta \leq \pi$), the capillary pressure is positive ($C > 0$). In the case of concave CB ($X > 1$, $0 \leq 1$, $0 \leq \theta < \pi/2$), the sign of C depends on the values of $X\sin\theta$. For instance, at $X \sin \theta < 1$, $C < 0$ (negative capillary pressure); at $C = 0$, and we have a CB catenoidal state. Zero capillary pressure is natural value for the classical catenoid [14], e.g. for capillary surface of soap mem-brane stretched between two coaxial rings, [15]. It is interesting to note, that the generatrix of CB with $C = 0$ differs from the classical catenoid generatrix (Fig. 3).

Two particular points on the positive branch of C worth atten-tion: At $C = 1/2$, CB acquires cylindrical shape with parameters $X = 1$ and $\theta = \pi/2$. Cylindrical CB is an attractive capillary subject because of its simple form, making the stability problems very transparent. The other reference point is $C = 1$, corresponding to spherical CB
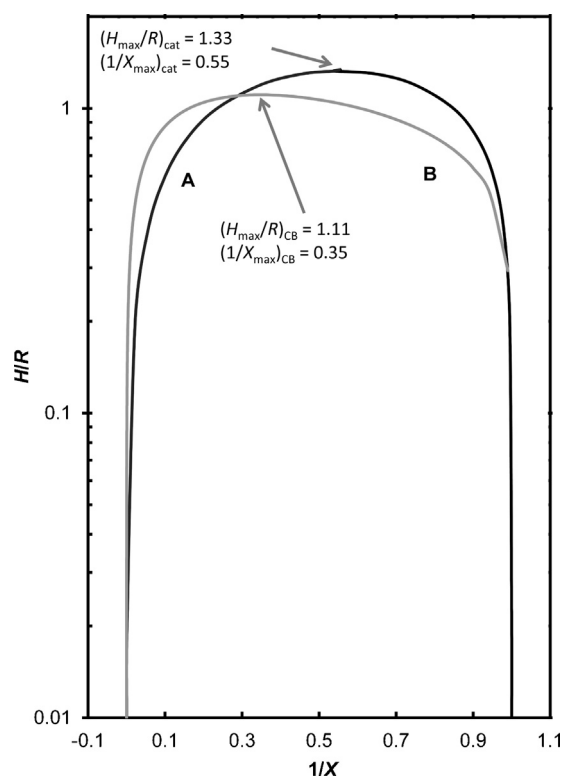
form (circular arc generatrix curve). From dynamic viewpoint, the spherical form corresponds to a CB state without supporting exter-nal force, $F = 0$ (see below) which some authors call 'equilibrium state' [16].

In the general case, capillary force F_γ acts upon the CB plates on part of the liquid, which if axisymmetric, will acquire the form:

$$F_\gamma = 2\pi R \gamma \sin \theta - \pi R^2 P_\gamma \qquad (3a)$$

The term $2\pi R \gamma \sin \theta$ is the normal (toward the contact plane) com-ponent of the three-phase contact force, and the term $\pi R^2 P_\gamma$ is the capillary pressure force. Upon expressing P_γ through C from Eq. (2) we finally obtain for F_γ:

$$F_\gamma = 2\pi R \gamma \frac{X - \sin \theta}{X^2 - 1} \qquad (3b)$$

By analogy with the parameter C, the force F_γ can alter its sign or become zero. At concave CB, since $X \geq 1$ for all angles in the inter-val $0 \leq \theta \leq \pi/2$, F_γ does not change its sign in the entire range of admissible values of the thickness H (see Section 3.3). It acts as an attractive force. The positive sign of the force according to Eq. (3b) in this case, $F_\gamma(X \geq 1) \geq 0$, is related to the sign of the external force F_e. The behavior of the force F_γ at convex CB is different. Since in this case $X < 1$, then F_γ is positive, i.e. attractive at $(\sin \theta - X) > 0$. In the point $\sin \theta = X$ the force is zero (spherical CB, see Eq. (2) at $C = 1$). The external force is negative at $X > \sin \theta$, i.e. $F_\gamma < 0$, repulsive force.

The static state (CB mechanical equilibrium) requires F_γ to be balanced by an external force F_e, ($F_e = F_\gamma$). The external force F_e here is regarded as positive when it is directed along the outer CB plates normal (Fig. 2). From experimental viewpoint this definition means that $F_e > 0$ is a stretching force, while $F_e < 0$ is a pressing force. We have to specify it in this way, because F_γ (in accord with the con-dition of equilibrium) has the reverse meaning, which could bring forth misconception.

3.2. Dynamic balance

A state of $F_e \neq F_\gamma$, will result motion of the plates (attraction or repulsion), with a force macrobalance of the kind:

$$F_{in} + F_\gamma + F_\eta = F_e \quad (4)$$

where F_{in} and F_η represent the inertial and viscous (drag) forces.

Under the conditions of the experiment (Section 2), the weight of the lower (mobile) plate played the role of an external force, $F_e = mg$ (m is the plate mass and g is the gravity constant). In the theoretical analysis, the liquid bridge weight is neglected, as it is much (some 100 times) smaller. For the same reason the inertia force can be assumed as $F_{in} = m\ddot{H}$, where $\ddot{H}$ is the acceleration of the plate. As we shall see from the experimental results (Section 4), $\ddot{H} \ll g$, so that F_{in} is negligible compared to the drag force, F_η. In this case, F_η has two components of resistance: in the bulk and in the three-phase contact line. At low Reynolds number, the drag force in the bulk can be presented in the form $F_b = B\dot{H}$ [17,18], with $\dot{H} = d|\Delta H|/dt$ and drag coefficient $B = \eta b$, where η is bulk viscosity coefficient. The factor b depends on the hydrodynamic boundary conditions and requires solution for each concrete case. The case of a thin CB the coefficient b will be considered in A (Eq. (10)). The resistance in the three phase contact line is a function of the three-phase contact line velocity ($\dot{R}$), but owing to the liquid incompressibility, $\dot{R}$ can be expressed through $\dot{H}$ (see e.g. Fig. 4a). At low values of the velocity $\dot{R}$, the contact line drag F_c obeys dependence similar to that for the bulk, $F_c = \eta_c b_c \dot{H}$, [19], where η_c and b_c are the respective coefficients.

3.3. Calculations

This section presents the mode of estimating the more important CB parameters as a function of height (see Fig. 4a and b). All calculations are based on the generatrix equation $y(x)$, for which Eq. (1) yields

$$y(x, C) = \frac{R I_0(x, C)}{X} \quad (5a)$$

where

$$I_0(x, C) = \pm \int_1^x \frac{1 + C(\xi^2 - 1)}{\sqrt{\xi^2 - \left[1 + C(\xi^2 - 1)^2\right]^2}} \, d\xi \quad (5b)$$

The integral $I_0(x,C)$ describes the upper part of the generatrix curve (above the equator, $y > 0$, see Fig. 4). The sign '±' accounts whether the CB is concave (positive sign, $X > 1$, $0 \leq \theta < \pi/2$) or convex (negative sign, $X < 1$, $\pi/2 < \theta \leq \pi$). Further the signs of I_0 will be omitted, accounting for the correct sign in every particular situation. Traditionally I_0 is presented via (Legendre's) elliptic integrals first and second kind F, E, [9], but for its evaluation we apply another calculation scheme (see further). The experimentally determinable parameter, related to I_0 is the CB height H:

$$H^* = \frac{2R^* I_0(X, C)}{X} \quad (6)$$

Both dimensionless parameters H^* and R^* are already scaled by the cube root of the CB liquid volume $V^{1/3}$, ($H^* = H/V^{1/3}$, $R^* = R/V^{1/3}$, see in Glossary). Note that $y(x, C)$ in Eq. (1) is scaled by r_m, i.e. $y(x, C) = z(r, C)/r_m$. As we already noted in Section 3.1, the scale $V^{1/3}$, known in the literature [16] accounts for the liquid incompressibility, thus making all results invariant from the initial droplet volume and its possible alterations in the course of the experiment, e.g. for evaporation. This scaling transforms the dimensionless expression for the volume into similar to Eq. (6) relation between the CB parameters:

$$1 = \frac{2\pi (R^*)^3 I_2}{X^3} \quad (7a)$$

where

$$I_2(X, C) = \int_1^X \frac{1 + C(\xi^2 - 1)}{\sqrt{\xi^2 - [1 + C(\xi^2 - 1)]^2}} \xi^2 \, d\xi \quad (7b)$$

Due to the obvious genetic connection (the same kernel) of the integrals, Eqs. (6) and (7b), they are marked as two members of the series:

$$I_n = \int_1^X \frac{1 + C(\xi^2 - 1)}{\sqrt{\xi^2 - [1 + C(\xi^2 - 1)]^2}} \xi^n \, d\xi, \quad \text{where} \quad n = 0, 2 \quad (8a)$$

We shall remind that in the dimension form the CB volume is given by the integral:

$$V = 2\pi r_m^3 \int_0^{H^*/2} x^2 \, dy \quad (8b)$$

The numerical procedure affects the computation of the integrals I_n. They are integrable, but singular (in the limit $X = 1$), which gives rise to significant instability of the numerical results. We have solved the problem by dividing the integrals into singular and regular parts. The singular part allows direct integration, while the regular part is estimated numerically. This procedure yields:

$$I_0(X, C) = \frac{\pi}{4C} - \frac{1}{2C} \arcsin \left[\frac{(1 - 2C) - 2C^2(X^2 - 1)}{(1 - 2C)} \right]$$
$$- \int_1^X \sqrt{\frac{x - [C(X^2 - 1) + 1]}{x + [C(X^2 - 1) + 1]}} \, dx \quad (9a)$$

$$I_2(X, C) = \left[1 + \frac{(1 - 2C)}{2C^2} \right] \frac{\pi}{4C} - \frac{\sqrt{(1 - 2C)(X^2 - 1) - C^2(X^2 - 1)^2}}{2C^2}$$
$$- \left[1 + \frac{(1 - 2C)}{2C^2} \right] \frac{1}{2C} \arcsin \left[\frac{1 - 2C - 2C^2(X^2 - 1)}{(1 - 2C)} \right]$$
$$- \int_1^X x^2 \sqrt{\frac{x - [C(x^2 - 1) + 1]}{x + [C(x^2 - 1) + 1]}} \, dx \quad (9b)$$

In practice, the estimate of I_n, according to Eqs. (9a) and (9b), is performed by assigning a series of values of X at a fixed contact angle θ. The computation procedure is split into two subintervals $X > 1$, $0 \leq \theta < \pi/2$ (concave CB) and $X < 1$, $\pi/2 < \theta \leq \pi$ (convex CB). The point $X = 1$, $\theta = \pi/2$ (cylinder), formally singular, is constructed directly (Fig. 4a). We have used for X step of $\Delta X = 0.05$; the angles subject to computation were: 1°, 7.5°, 15°, 30°, 45°, 60°, 89°, 89.9°, 90.2°, 91°, 120°, 135°, 150°, and 179° (Fig. 4a).

4. Results and discussion

In this section we shall discuss results related to static and dynamic CB. The comments on static CB are subdivided, for concave and convex CB (see Section 2), and comprise both experimental and theoretical results.

4.1. Static capillary bridges

The key result of the static CB experiments is on the verification of the agreement between computed and measured CB geometric parameters (H, R, r_m, θ). Additional information about the contact angle hysteresis and the upper stretching limit (H_{max}) is provided.

4.1.1. Concave CB, $0 \leq \theta < \pi/2$

The experimental data are presented in Fig. 5. The coordinate system (H/R) vs. X^{-1} is so chosen as to allow using the measurable parameters H, R и r_m in any arbitrary scale. In addition, the coordinate X^{-1} has been favored for more compact presentation
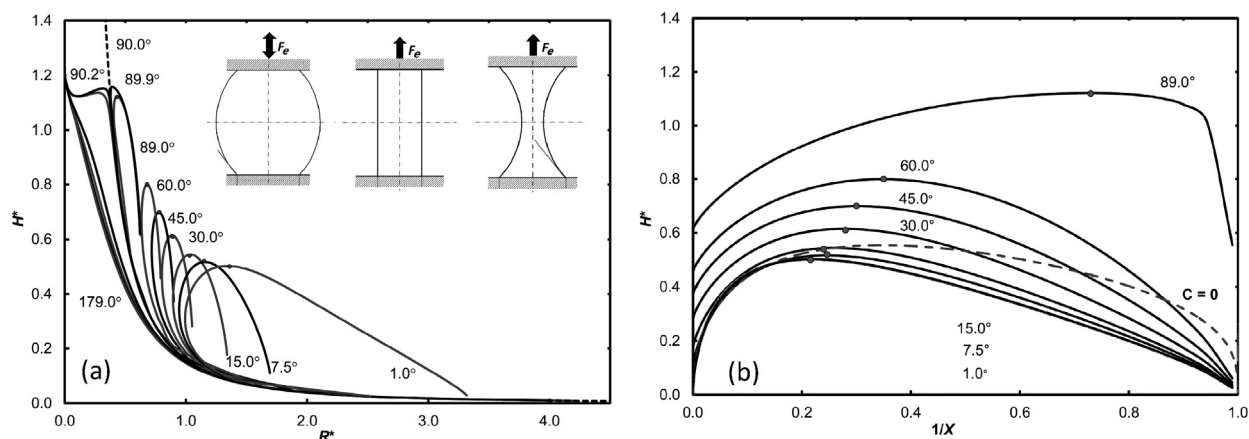
Fig. 4. Selected isogonic plots: (a) dimensionless height, H^* vs. dimensionless contact radius R^* and (b) H^* vs. $1/X$. The isogonic maxima $H^*_{max}(\theta)$ on the plots (a) and (b) are equal for the corresponding contact angles θ (see the points). The thermodynamic branch is on the left-hand side and below H^*_{max} in the plot (a), and on the right branch in the plot (b). $C=0$ represents the catenoidal state. The inset shows the direction of the external force, F_e.

$(0 \leq X^{-1} \leq 1)$ than the parameter $X (1 \leq X < \infty)$. Concurrently, the co-ordinate (H/R) complicates the interpretation of the data. Thus, for example, the maximum $(H/R)_{max}$ is not a stretching limit point. It does not correspond to the maximum $(H^*)_{max}$ (Fig. 4b). The experimental observation confirms this fact. The data points in Fig. 5 exceed $(H/R)_{max}$ but not the real stretching limit (the black points on the isogones). As expected, the comparison with the data of the plots in Fig. 5 and Fig. 4 confirms that they lie on the thermodynamic branch of the isogones.

The measured contact angles are in good agreement with the angles of the computed isogones (see the marked values 41°, 55°, Fig. 5). As is seen from the graph, the concave CB exhibits expressed hysteresis. Starting from contact angles values of $\theta = 55$–60° for the thin CB $(X^{-1} \cong 0.85)$, upon their stretching the angles diminish to about $\theta = 32°$ and $X^{-1} \cong 0.7$. Further they increase again to about $\theta \cong 45°$ and $X^{-1} \cong 0.3$. The contact angles passage through a minimum is further proof for the theoretical analysis. Qualitatively, this can be illustrated by drawing vertical line (pinned contact, $R^* = const$) for each measured value of R, in Fig. 4a. The points of

intersection with the corresponding isogone mark the dependence $\theta(H^*, R^* = const)$.

4.1.2. Convex CB, $(\pi/2 < \theta < \pi)$

The experimental data on convex CB are presented in Fig. 6. The coordinate X was chosen (instead of X^{-1}, see Fig. 5) for the sake of convenience of the analysis. Within the relatively narrow range of $X = 0.99$–0.91 the data practically lie on a single isogone of $\theta \approx 100°$, and they do not exhibit detectable hysteresis. The observed deviation from the isogone we attribute to the effect of gravity, in the range X = 0.91–0.8.

The series of photos above in the graph (Fig. 6) show that the deviation coincides with the rise of observable difference between the upper and lower radii of contact. In accord with the expected gravitational influence, the upper radius (and angles) of contact diminish, while the corresponding parameters on the lower plate augment. It is a fact of interest that the mean angle values of the two (upper and lower) contacts remain practically constant, $\theta \approx 100°$ over the entire range of CB existence. The domain of
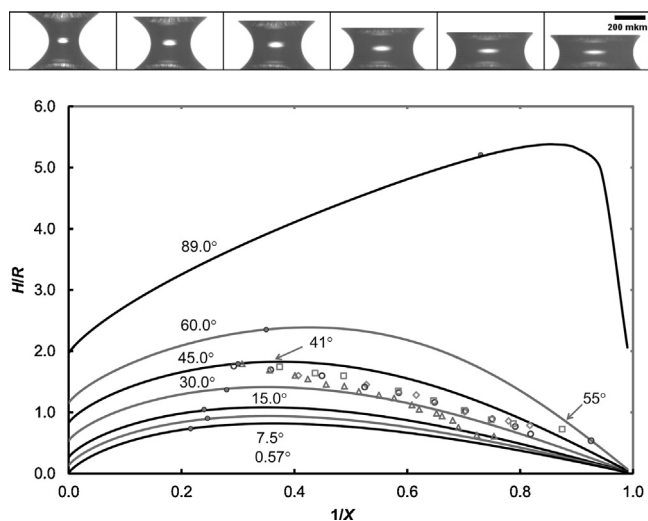
Fig. 5. Data from several experiments (the triangles, hollow circles and squares) of concave CB stretching (direction of stretching is from right to left). The measured contact angles indicated apparent hysteresis. The photo series above illustrate the real CB shape deformation at stretching.
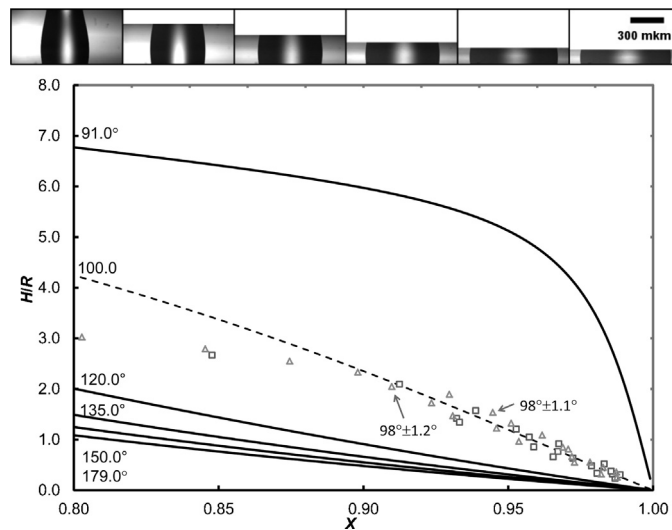
Fig. 6. Data from two experiments (triangles and squares) of convex CB (direction of stretching is from right to left). The contact angle at weak stretching ($X = 0.99$–0.91) is practically constant. The deviation from the isogone at stronger stretching is due to gravity. The photo series above illustrate the real CB shape deformation at stretching.
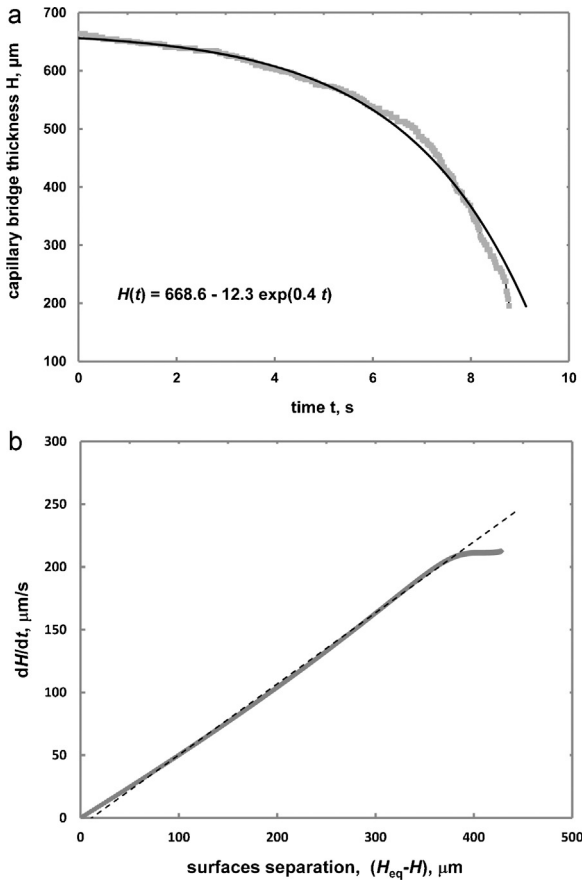
Fig. 7. Experimental data of concave CB capillary pressing/attraction: (a) CB thickness H vs. time t and (b) thinning velocity dH/dt vs. $(H_{eq} - H)$, (see the text).

rupture (the upper existence limit) of the investigated convex CB turned to be at $X = 0.84$–0.80, significantly earlier than the definition limit $X = 0$ (Appendix A). This is another significant difference from the concave CB, where the maximum height, H^*_{max} is practically reached (Fig. 5). The reason for the premature rupture could be the rise of Rayleigh instability [20], combined with the gravitational deformation. Yet, this phenomenon requires its own analysis.

4.2. Dynamic capillary bridges

The scheme of the dynamic experiments is given in Section 2.2 and the results are shown in Fig. 7a and b. The motion quality is clearly outlined in two dependences, presented there, but the 'velocity vs. ΔH' is the more informative. H_{eq} is the equilibrium thickness in the abscissa and $\Delta H = H_{eq} - H$. As described in Section 2.2, H_{eq} can be clearly established experimentally. The force balance of this state $F_\gamma(H_{eq}) = F_e$ results from Eq. (4). It determines the parameters of the static pending CB (H_{eq}, etc.) through Eqs. (3a), (6), and (7). Since the motion is initiated by slightly pressing the top plate, and thus decreasing the CB thickness, ΔH turns into a natural coordinate of the process. The rectilinear section of the relationship in Fig. 7b corresponds to $\Delta H(t)$ dependence, $\ln(\Delta H) \sim t$ (Fig. 7a). The subsequent negative deviation suggests viscous effects prevailing over the driving capillary force changes. The straight-line section in the 'velocity vs. ΔH' graph (Fig. 7b), results from the general Eq. (4), at the following approximations:

Firstly, the experiment specifies that the inertia (in the rectilinear section) is negligible. As shown in Section 3.2, it suffices

for the purpose to show that $\ddot{H} \ll g$. The estimate of the inertia term in Eq. (4) is performed by equivalently expressing $\ddot{H} = \dot{H} d\dot{H}/d(\Delta H)$ and introducing the orders of magnitude of the respective quantities from Fig. 7b, e.g. $\dot{H} \leq 200 \,\mu m$, $d\dot{H}/d(\Delta H) \approx 0.5\, s^{-1}$, i.e. $\ddot{H} \leq 100 \,\mu m/s^2$. In the same scale $g \approx 10^7 \,\mu m/s^2$, which perfectly justifies neglecting of the inertia term. Thus, three terms remain significant in the force balance Eq. (4), namely, the capillary force F_γ, the viscous force F_η, and the gravity force of the plate mg:

$$F_\gamma + F_\eta = mg \tag{10}$$

Secondly, the approximation, given below, is valid for the initial stage of the process (near the static state):

$$F_\gamma(H_{eq} - \Delta H) - mg \approx -\left(\frac{\partial F_\gamma}{\partial H}\right)_{eq} \Delta H \tag{11}$$

Expressing the friction force by $F_b = B\dot{H}$ (Section 3.2) turns Eq. (10) into:

$$B\dot{H} = \left(\frac{\partial F_\gamma}{\partial H}\right)_{eq} \Delta H \tag{12}$$

Eq. (12) describes qualitatively the rectilinear section of the experimental dependence in Fig. 7b. Yet, proving the model demands further quantitative experimental corroboration of the value of the coefficient of proportionality $(\partial F_\gamma/\partial H)_{eq}/B$, which requires further investigation. Considering the deceleration in the later stages of CB thinning, as we already noted, it is mostly due to specific aspects in the dependences $F_\gamma(H)$, $F_\eta(H)$. In the literature can be found reports dedicated to similar problems. Each of them more or less is devoted to a particular case [21–24]. We suggest that the dynamics of thin CB fits the discussion in Refs [25,26].

4.3. Thin liquid bridge

In contrast to the variety of CB profiles near the upper height limits, their flattening (thinning) toward zero thickness (the lower CB limit), is of much more universal character. This universality starts to show itself at a thickness H much smaller than the radius of contact R ($R \gg H$). It offers the ground to set the thin capillary bridges into a separate domain of their own. Since thin CB is situated in the region $R^*, r, r^*_m \to \infty$, the analysis by means of the X-coordinate is more convenient. Taking into account the definition $X \equiv R^*/r^*_m$, and the self-evident fact that for the thermodynamic branch, $X(R^* \to \infty) \to 1$ makes suitable the substitution $X = 1 + \Delta$, at $\Delta \to 0$. Thus, the parameter C (dimensionless capillary pressure, Eq. (2)) in the thin CB region tends to:

$$C(X = 1 - \Delta) \approx \sim -\frac{1 - \sin\theta}{2\Delta} + \frac{1 + \sin\theta}{4} \tag{13}$$

The two terms on the right-hand side represent the two (dimensionless) curvatures: the generatrix curvature, also named meridional curvature (first term) and the azimuthal curvature (second term). For example, at $\theta = 90°$ we obtain a cylinder; the generatrix turns into a straight line of zero curvature, which leaves only the second (azimuthal) curvature, equal to 1/2 and $C = 1/2$. The generatrix curvature change of sign as a function of the contact angle is allowed for by the sign of Δ.

It is worth commenting on the fact that the thin CB generatrices converge to equations of circular peripheries, which follows from Eq. (5). The latter in the approximation of a thin CB, $1 \leq x \leq 1 + \Delta$ takes the form:

$$\frac{dy}{dx} = -\frac{1 + 2C(x-1)}{\sqrt{1 - [2C(x-1) + 1]^2}} \tag{14}$$

Upon integration, Eq. (14) yields:

$$y^2 + (x + 1 - X_c)^2 = X_c^2 \qquad (15)$$

The dimensionless circular radius $X_c = 1/2C$ (coinciding with the CB generatrix radii of curvature) is related to the CB thickness, via $H/2r_m = X_c|\cos\theta|$. The use of modulus sign is meant to eliminate the sign alteration when the angle θ passes through $\pi/2$ (see above). The capillary pressure, C is represented by the first term on the right-hand side of Eq. (13). Eq. (15) can be generalized as

$$y^2 + (x - 1 \pm X_c)^2 = X_c^2 \qquad (16)$$

where the positive sign is for $\theta < \pi/2$ and negative for $\theta > \pi/2$.

Estimation of the capillary force acting upon thin CB yields the respective asymptotic formula for F_γ:

$$F_\gamma(X = 1 + \Delta) \approx \pi\gamma R \left(1 + \frac{1 - \sin\theta}{\Delta}\right) = \pi\gamma R \left(1 + 2R\frac{\cos\theta}{H}\right) \qquad (17)$$

By analogy to the capillary pressure, again for the case of $\theta \neq 90°$, the second term in the right hand side is of interest, which eventually (upon sufficient thinning) becomes dominant $F_\gamma(H \to 0) = 2\pi\gamma R^2 \cos\theta/H$. Allowing for the volume constancy ($\pi R^2 H = $ const), makes the force F_γ in the asymptotic dependence inversely proportional to the thickness of a square: $F_\gamma(H \to 0) \sim 1/H^2$. In the estimate of the volume, we have assumed that it equals to its cylindrical part, disregarding the menisci- an entirely correct approximation in case of sufficiently thin bridges.

The initiated dynamic analysis sets the interesting question about the spontaneous evolution of CB with wetting liquid (e.g. water between glass plates). Naturally, the weight of the plates is an inevitable force component, but below certain thickness it can be definitely disregarded. The wetting will cause progressive thinning and the eventual formation of a thin bridge. Yet, the thinning of a thin liquid layer between parallel plates is a well-studied problem in hydrodynamics, for which the law of viscous friction (Reynolds law) is valid: $F_\eta = 3\dot{H}\eta R^4/8H^3$ ($\dot{H}$, thinning rate and η, viscosity), [27,28]. Applying again the postulate of constant volume, for the friction force, we arrive at a (similar to that of the capillary force) simple dependence on thickness: $F_\eta \sim \dot{H}\eta/H^5$. The next natural step is to set the wetting force F_γ equal to the friction force F_η, in order to describe the CB kinetics of thinning: $\dot{H} \sim H^3$. We must stipulate here that, similarly as at the estimate of the volume, the resistance at the edges of the thinning bridge is neglected in the Reynolds formula. The analysis can be extended further by taking into account that $\dot{H} = -dH/dt$, with subsequent integration.

The deceleration in the later stages of CB thinning, as we already noted is mostly due to specific aspects in the dependences $F_\gamma(H)$ and $F_\eta(H)$. General theory is not yet developed, but we shall give an indicative example. Section 3.3 provides a relation of the kind (9α), valid for thin CB, $\dot{H} \sim H^3$, which in terms of ΔH states:

$$\dot{H} \sim (H_{eq} - \Delta H)^3 \qquad (18)$$

As Eq. (18) shows, the slope of the 'velocity vs. ΔH' dependence is already negative.

5. Conclusion

As is natural for a study dedicated to a classical subject, the contributions in the present one about the capillary bridges are mainly methodological. One relatively little investigated aspect here is the so-called CB 'definition domain', i.e. the interval of parameter values in which the CB equations hold (Appendix A). This problem has been analyzed on reversible CB model engaging bridges which maintain the contact angle constant at stretching or pressing. The most expressed and experimentally manageable parameter is the CB height (thickness) H, presented in the form of isogone ($\theta = $ const) in different co-ordinate systems (e.g. Fig. 2a and b). The computed isogones exhibit differences in the behavior of concave and convex CB. Both the concave and the convex CB are characterized by an upper thickness limit. With concave CB the upper limit is a maximum in the respective isogone [a function of the contact angle $H_{max}(\theta)$], while the upper thickness limit of a convex CB is constant in the entire range of obtuse contact angles, $\pi/2 < \theta \leq \pi$ (Fig. 2). Another difference between concave and convex CB is observed in the behavior of the contact radius, $R(H, \theta = $ const). With concave CB the radius R passes through a minimum which is dependent on the contact angle $R_{min}(\theta)$, while with convex CB, the contact radius steadily reduces to zero (Fig. 2). The boundary $R(\theta \neq \pi) = 0$ has proved attainable, due to the formation of an inflexion on the convex CB generatrix.

Differences in the concave and convex CB behavior have been observed also at (quasi-) static experiments. For example, concave CB exhibit pronounced hysteresis (isogones crossing at stretching; Fig. 5), while convex CB stayed practically on the same isogone, $\theta = $ const (Fig. 6). The capacity of the method to study the hysteresis at stretching normal to the plates designates one of the chief directions of our future experiments. The observed realization of the upper height limit also deserves attention. Concave CB closely approaches the theoretical limit $H_{max}(\theta)$ (Fig. 5), while convex CB breaks definitely earlier (Fig. 6). Most generally, these facts indicate that destabilizing effects arise at the convex bridges, one of which is observed in the appearance of inflexion. We shall remind here that the stability problems are beyond the scope of the present investigation; hence the comments as made are of hypothetical nature. Yet, the observations on the thinning kinetics of concave bridges (Section 4.2) are of markedly pioneer significance. The obtained results show exponential time dependence $\Delta H(t)$ it the first stage, followed by distinct deceleration of the process. The proposed interpretation of this dynamics, which is still at the stage of modeling, undergoes presently its development in direction to a quantitative theory.

Appendix A. Definition domain of capillary bridge

The interval of parameter values satisfying Eqs. (5) and (7) should be conceived as the CB definition domain. In Figs. 3 and 4, this relation is represented in different co-ordinates in the form of isogones (constant contact angle families). A characteristic of the isogones in the range of $0 \leq \theta < 90°$ is the existence of a maximum in the co-ordinate proportional to the height H (independent of scaling). In Fig. 4a and b, the dependence of the maximal height on the contact angle, $H^*_{max}(\theta)$, is clearly visible. Naturally, the values of $H^*_{max}(\theta)$ are the same for a particular angle values in the diagrams on Fig. 4a and b, regardless of the different abscissae values. The diagrams of cylinder ($\theta = 90°$) indicate unlimited height, i.e. $H \to \infty$. This behavior of the cylinder is due to the characteristics of its shape, straight line generatrix, permitting zero contact radius limit ($R \to 0$). The isogones heights in the range $90° < \theta \leq 180°$ are also limited with respect to stretching, but for quite different circumstances. All isogones here end at a point contact $R^* = 0$ (Fig. 4a). It is interesting to note that in the state of $R^* = 0$ the parameter C acquires the value $C(X=0)=1$, independent on the contact angle value, Eq. (2), and coinciding with the value of C for a sphere (Section 3.1). The similarity of the point
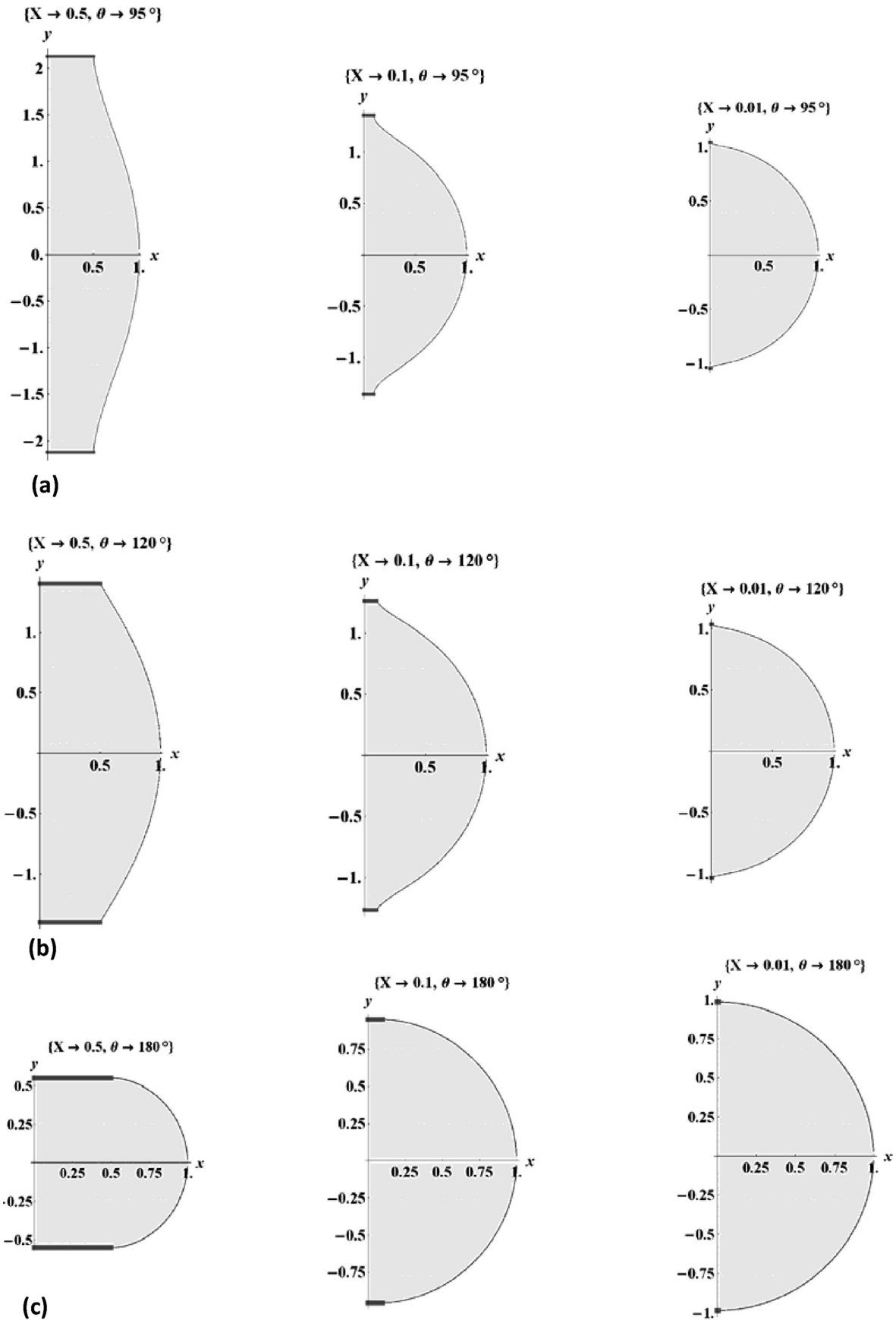
Fig. A.1. Capillary bridge profiles computed for three different states ($X = 0.01, 0.1, 0.5$) of three isogones in dimensionless coordinates $y = y(x)$: (a) $\theta = 95°$; (b) $\theta = 120°$; and (c) $\theta = 180°$. The appearance of an inflexion is distinctly perceptible at increased stretching ($X = 0.1, 0.5$) at $\theta \neq 180°$.

Table A.1
Inflection points coordinates, x_i for angles 95°, 120° at different stretching.

Parameters	θ	95°			120°		
	X	0.50	0.10	0.01	0.50	0.10	0.01
x_i		0.70	0.32	0.10	0.57	0.29	0.10

$R^* = 0$ with the spherical CB-shape is deepened by the calculated value $H^*(R^* = 0) \cong 1.24$. Indeed, when expressing the height H from the definition $H^* \equiv H/V^{1/3}$, and assuming it equal to the sphere diameter ($V = \pi H^3/6$), we obtain $H^* = (6/\pi)^{1/3} = 1.24$. The problem here is that the complete (closed) sphere is only congruent with a contact angle $\theta = 180°$ while for all other angles the asymptote $R \to 0$ calls for additional analysis. The solution of the problem is associated with the appearance of an inflexion point x_i in the generatrix, i.e. with the appearance of a root in $(d^2y/dx^2)_{x_i} = 0$, Eq. (5):

$$x_i^2 = \frac{1 - C}{C} = X\frac{\sin\theta - X}{1 - X\sin\theta} \qquad (A.1)$$

The result (A.1) is known in the literature [9], but is not analyzed parametrically. It ensues from Eq. (A.1) that the inflexion emerges in the range $0 < X < \sin\theta$, i.e. beyond the 'sphere' state (Section 3.1). Another obvious consequence of Eq. (A.1) is that an inflexion does not appear at $\theta = 180°$, but the point contact there is realized through a closed sphere (see above). As for the point contact at $\theta \neq 180°$, formally it looks as a kink point on the liquid surface, but its correct interpretation is as a three-phase contact point.

Fig. A.1 illustrates the presence of an inflexion point for two angles (95°, 120°) at different X (different stretching). It is clearly seen that at $\theta = 180°$ any signs of inflexion are absent. The x_i values, calculated according to Eq. (A.1) and coinciding with the points of the graphs, are presented in Table A.1:

The lower (zero) limit of CB height ($H \to 0$) is accessible to all isogones at $0° \leq \theta \leq 180°$ (see Fig. 4). For details about the CB behavior at $H \to 0$, see Section 4.3.

It is worth considering the two branches around H_{max}^* (Fig. 4a and b). We shall note the fact that such a duality as $H^*(R_1^*) = H^*(R_2^*)$, Fig. 4a; $H^*(1/X_1) = H^*(1/X_2)$, Fig. 4b, is observed only at concave CB. Both are equilibrium branches (solution of Eq. (3.1)), but of different surface energy. The analysis reveals that the branch corresponding to lesser X at $H = $ const (the right-hand side branch in Fig. 4b) is of smaller surface energy, i.e. the (thermodynamically) equilibrium branch. From geometrical viewpoint, CB of a smaller X value looks less taken in at the waist. Similar dual trend of the capillary surface generatrix has been established already at the catenoid. Fig. 3 shows the graphs of a classical catenoid and of CB at $C = 0$. The right-hand sides (of smaller X) correspond to the thermodynamically stable branches on both graphs.

We shall finally refer to the contact radius R definition domain. Informative to the purpose are the diagrams H^* vs. R^* in Fig. 3. In this case the left-hand side toward the maximum represents the thermodynamic branch. Their specificity is that when descending along given isogone from H_{max} down to smaller thicknesses, the contact radius R initially decreases [$(\partial R/\partial H)_\theta > 0$]. This paradoxical (from the standpoint of liquid incompressibility) course persists as long as reaching certain minimal radius, $(\partial R/\partial H)_\theta = 0$, after which R alters its course in 'natural' direction $(\partial R/\partial H)_\theta < 0$. Obviously, constant volume in the region $H(R_{min}) \leq H \leq H_{max}$ is maintained on the account of r_m, which exhibits continuous alteration $(\partial r_m/\partial H)_\theta < 0$ for all H values.

Appendix B. Glossary

Denotation	Description	Sections, Eqs., Figs.
Dimension symbols		
r, z	Current coordinates	Section 3.1, Eq. (1)
		Section 3.3, Fig. 2
r_m, R	Waist (neck), contact radii	Section 3.1, Fig. 2
φ, θ	Current, contact angles	Section 3.1, Fig. 2
H, V	Height (thickness), volume	Section 3.3, Fig. 2
$F_{in}, F_\gamma, F_\eta, F_e$	Inertia, capillary, viscous (drag), external (supporting) forces	Section 3.1, Fig. 2 Section 3.2, Eq. (4),
P_e, P_i, P_γ	External, internal, capillary pressures	Section 3.1, Fig. 2
γ	Surface tension	Section 3.1
Dimensionless (scaled by r_m) symbols		
$x; y$	Current coordinates	Section 3.1
$X; C$	Contact radius, capillary pressure	Section 3.1, Eq. (2)
Dimensionless (scaled by $\sqrt[3]{V}$) symbols		
r_m^*, R^*, H^*	Waist, contact radii, height	Section 3.3, Eq. (6)

References

[1] J. Plateau, Statique expérimentale et théorique des liquides soumis aux seules forces moléculaires, Gauthier-Villars, 1873.
[2] Y. Men, X. Zhang, W. Wang, Capillary liquid bridges in atomic force microscopy: formation, rupture, and hysteresis, J. Chem. Phys. 131 (2009), 184702–184702-8.
[3] D.J. Broesch, J. Frechette, From concave to convex: capillary bridges in slit pore geometry, Langmuir 28 (2012) 15548–15554.
[4] L. Vagharchakian, F. Restagno, L. Léger, Capillary bridge formation and breakage: a test to characterize antiadhesive surfaces, J. Phys. Chem. B 113 (12) (2009) 3769–3775.
[5] Y. Wang, S. Michielsen, H.J. Lee, Symmetric and asymmetric capillary bridges between a rough surface and a parallel surface, Langmuir 29 (2012) 11028–11037.
[6] J.-P. Gras, J.-Y. Delenne, M.S. El Youssoufi, Study of capillary interaction between two grains: a new experimental device with suction control, Granular Matter 15 (2013) 49–56.
[7] D.T. Thi, A.T. Fomenko, Minimal surfaces, stratified multivarifolds, and the plateau problem, in: AMS, Translations of Mathematical Monographs, 1985, pp. 84.
[8] T.I. Vogel, Stability of a liquid drop trapped between two parallel planes, SIAM, J. Appl. Math. 47 (3) (1987) 516–525.
[9] P. Kralchevsky, K. Nagayama, Particles at Fluid Interfaces and Membranes, Elsevier, Amsterdam, 2001.
[10] K.G. Marinova, D. Christova, S. Tcholakova, E. Efremov, N.D. Denkov, Hydrophobization of glass surface by adsorption of polydimethylsiloxane (PDMS), Langmuir 21 (2005) 11729–11737.
[11] R.D. Deegan, O. Bakajin, T.F. Dupont, G. Huber, S.R. Nagel, T.A. Witten, Capillary flow as the cause of ring stains from dried liquid drops, Nature 389 (1997) 827–829.
[12] R.D. Deegan, O. Bakajin, T.F. Dupont, G. Huber, S.R. Nagel, T.A. Witten, Contact line deposits in an evaporating drop, Phys. Rev. E 62 (2000) 756–765.
[13] F. Girard, M. Antoni, S. Faure, A. Steinchen, Evaporation and Marangoni driven convection in small heated water droplets, Langmuir 22q (2006) 11085–11091.
[14] N.M. Princen, The equilibrium shape of interfaces drops, and bubbles. Rigid and deformable particles at interfaces, in: E. Matijievich (Ed.), Surface and Colloid Science 3, Wiley, New York, 1969, pp. 1–83.
[15] M. Ito, T. Sato, In situ observation of a soap-film catenoid – a simple educational physics experiment, Eur. J. Phys. 31 (2) (2010) 357–365.
[16] H. Kusumaatmaja, R. Lipowsky, Equilibrium morphologies and effective spring constants of capillary bridges between structured surfaces, Langmuir 26 (24) (2010) 18734–18741.
[17] J. Happel, H. Brenner, Low Reynolds Number Hydrodynamics with Special Applications to Particulate Media, Prentice-Hall, New Jersey, 1965.
[18] G.K. Batchelor, An Introduction to Fluid Mechanics, Cambridge University Press, Cambridge, 1974.
[19] T.D. Blake, Y.D. Shikhmurzaev, Dynamic wetting by liquids of different viscosity, J. Colloid Interface Sci. 253 (2002) 196–202.
[20] J.W. Strut Lord Rayleigh, On the instability of jets, Proc. London Math. Soc. 10 (1878) 4–13.
[21] P.G. Saffman, Brownian motion in thin sheets of viscous fluid, J. Fluid Mech. 73 (1976) 593–602.
[22] B.D. Hughes, B.A. Pailthorpe, L.P. White, The translational and rotational drag on a cylinder moving in a membrane, J. Fluid Mech. 110 (1981) 349–372.
[23] O.V. Voinov, Hydrodynamics of wetting, Fluid Dyn. 11 (1976) 714–721.
[24] P.G. de Gennes, Wetting: statics and dynamics, Rev. Mod. Phys. 57 (1985) 827–863.

[25] R. Dimova, K. Danov, B. Pouligny, I. Ivanov, Drag of a solid particle trapped in a thin film or at an interface: influence of surface viscosity and elasticity, J. Colloid Interface Sci. 226. (2000) 35–43.

[26] K. Danov, R. Dimova, B. Pouligny, Viscous drag of a solid sphere straddling a spherical or flat surface, Phys. Fluids 12 (10) (2000) 2711–2723.

[27] O. Reynolds, On the theory of lubrication and its application to Mr. Beauchamp Tower's experiments including an experimental determination of the viscosity of olive oil, Philos. Trans. 177 (1866) 157.

[28] B.P. Radoev, D.S. Dimitrov, I.B. Ivanov, Hydrodynamics of thin liquid films. Effect of the surfactant on the rate of thinning, Colloid. Polym. Sci. 252 (1974) 50–55.